


# MRI-based whole-brain elastography and volumetric measurements to predict brain age

Claudio Cesar Claros-Olivares<sup>1,†</sup>, Rebecca G. Clements<sup>2,3,4,†</sup>, Grace McIlvain<sup>2,5</sup>, Curtis L. Johnson <sup>1,2,\*</sup> and Austin J. Brockmeier<sup>1,6,\*</sup>

<sup>1</sup>Department of Electrical & Computer Engineering, University of Delaware, Newark, DE 19716, United States

<sup>2</sup>Department of Biomedical Engineering, University of Delaware, Newark, DE 19713, United States

<sup>3</sup>Department of Biomedical Engineering, Northwestern University, Evanston, IL 60208, United States

<sup>4</sup>Department of Physical Therapy and Human Movement Sciences, Northwestern University, Chicago, IL 60611, United States

<sup>5</sup>Department of Biomedical Engineering, Columbia University, New York, NY 10027, United States

<sup>6</sup>Department of Computer & Information Sciences, University of Delaware, Newark, DE 19716, United States

\*Corresponding author. Department of Electrical & Computer Engineering, University of Delaware, 140 Evans Hall, The Green Newark, DE 19716, USA.

E-mail: [ajbrock@udel.edu](mailto:ajbrock@udel.edu) (A.J.B.); Department of Biomedical Engineering, University of Delaware, 540 S College Ave, Newark, DE 19713, USA. E-mail: [clj@udel.edu](mailto:clj@udel.edu) (C.L.J.)

<sup>†</sup>Contributed equally as first author.

## Abstract

Brain age, as a correlate of an individual's chronological age obtained from structural and functional neuroimaging data, enables assessing developmental or neurodegenerative pathology relative to the overall population. Accurately inferring brain age from brain magnetic resonance imaging (MRI) data requires imaging methods sensitive to tissue health and sophisticated statistical models to identify the underlying age-related brain changes. Magnetic resonance elastography (MRE) is a specialized MRI technique which has emerged as a reliable, non-invasive method to measure the brain's mechanical properties, such as the viscoelastic shear stiffness and damping ratio. These mechanical properties have been shown to change across the life span, reflect neurodegenerative diseases, and are associated with individual differences in cognitive function. Here, we aim to develop a machine learning framework to accurately predict a healthy individual's chronological age from maps of brain mechanical properties. This framework can later be applied to understand neurostructural deviations from normal in individuals with neurodevelopmental or neurodegenerative conditions. Using 3D convolutional networks as deep learning models and more traditional statistical models, we relate chronological age as a function of multiple modalities of whole-brain measurements: stiffness, damping ratio, and volume. Evaluations on held-out subjects show that combining stiffness and volume in a multimodal approach achieves the most accurate predictions. Interpretation of the different models highlights important regions that are distinct between the modalities. The results demonstrate the complementary value of MRE measurements in brain age models, which, in future studies, could improve model sensitivity to brain integrity differences in individuals with neuropathology.

**Keywords:** convolutional neural networks; deep learning; elastography; magnetic resonance imaging; neuroimaging; neuroscience

## Introduction

The brain changes in structural integrity, functional connectivity, tissue anisotropy, and synaptic plasticity across the lifespan, with tissue degeneration rapidly accelerating in older adults [1–3]. Understanding the natural progression of brain changes is critical for establishing brain biomarkers of atypical development and degeneration. Advanced neuroimaging techniques capable of measuring the structural integrity of neural tissue offer sensitive metrics that reflect glial matrix organization, neuronal density, and myelination. One such method is magnetic resonance elastography (MRE), which is a phase contrast magnetic resonance imaging (MRI) technique that has gained notability over the past decade as the most robust noninvasive method for quantifying brain mechanical properties. MRE creates whole-brain, high-resolution maps of tissue viscoelastic shear stiffness and damping ratio. These properties are sensitive to tissue microstructural composition and organization and demonstrate age-related

changes during both neurodevelopment and neurodegeneration, with softening occurring across the life span [4–6]. The age-related softening of the brain can be exacerbated by neurodegenerative diseases such as Alzheimer's disease, multiple sclerosis, and Parkinson's disease [6–10].

The sensitivity of mechanical properties to tissue integrity makes them strong candidates as metrics for predicting brain health from imaging data. Age-related brain tissue softening has been well studied with MRE, with previous works reporting that the global brain softens with age at a rate of around 0.3%–1% per year [11] and that the specific softening rate varies among brain regions [4, 12–17]. Similar regional, age-related differences have been reported in developing populations, and attributed to synaptic pruning and reorganization of myelin and glial cells [18–20]. These microstructural changes are of interest across the life span as they give rise to changes in cognitive function in both healthy individuals and in cases of pathology—reflecting the sensitivity of tissue mechanics to tissue health. However, nearly

Received: 15 July 2024. Revised: 3 November 2024. Editorial decision: 4 November 2024. Accepted: 12 November 2024

© The Author(s) 2025. Published by Oxford University Press.

This is an Open Access article distributed under the terms of the Creative Commons Attribution-NonCommercial License (<https://creativecommons.org/licenses/by-nc/4.0/>), which permits non-commercial re-use, distribution, and reproduction in any medium, provided the original work is properly cited. For commercial re-use, please contact [reprints@oup.com](mailto:reprints@oup.com) for reprints and translation rights for reprints. All other permissions can be obtained through our RightsLink service via the Permissions link on the article page on our site—for further information please contact [journals.permissions@oup.com](mailto:journals.permissions@oup.com).

all prior work relating MRE measurements to age have used pre-selected regions-of-interest (ROIs), summarizing the mechanical properties in each ROI, and have not taken advantage of the rich, whole-brain mechanical property maps that MRE can provide.

The ultimate goal of brain age prediction is to detect deviations between chronological age and predicted age as an indicator of abnormal brain health, and pinpoint the cause in the brain measurements. Imaging modalities including diffusion-weighted, functional, and structural MRI have already shown promising results for brain age prediction [21–24]. The use of supervised machine learning to predict chronological age by extracting features from neuroimaging data and correlating them to age is well established [25, 26]. To process whole-brain maps, deep learning architectures, such as convolutional neural networks (CNNs), have become increasingly prevalent in neuroimaging studies, including those focused on predicting brain age [27–32]. Soumya Kumari and Sundarajan [33], for example, reported an evaluation of 32 different brain age prediction models ranging from traditional to deep learning methods. Similarly, Tanveer et al. [34] reviewed 35 studies that applied deep learning techniques for brain age prediction, with 25 using models, such as 3D CNNs, applied to whole brain 3D images (voxel-based), and the remaining 10 studies using models for the 2D image slices. More generally, 3D CNNs are widely used in medical imaging applications, including tumor detection, disease progression prediction, image segmentation, and image reconstruction [35–38].

Here, we propose to incorporate whole-brain MRE measurements into brain age models through 3D CNNs. The models learn to predict a subject’s chronological age from different combinations of whole-brain measurements, combining the MRE mechanical properties and structural volume as a stack of 3D maps all registered to a common template. We select network architectures already reported in the literature that accept multiple 3D brain maps as input (ResNet [39] and SFCN [40]). To better understand the benefits of using a 3D CNN, we compared to traditional statistical approaches as baseline regression models (ElasticNet regularization and Random Forest (RF)). To interpret the networks, we use a method for computing spatial saliency maps of the trained networks’ internal features to understand the spatial location of predictive features [41].

Given that MRE is still an emerging neuroimaging technique and previously published sample sizes are relatively small, we pooled data from multiple studies employing similar imaging and processing protocols, as has been previously done by Hiscox et al. [42], creating splits to test whether models trained on a subset of studies generalize to unseen studies. We include data from healthy subjects of varying ages, including children, adolescents, young adults, and older adults (Fig. 1). In this healthy population, we assume that brain age equals chronological age, and the goal is to optimally predict chronological age from maps of brain structure and mechanical properties. Ultimately, a well-trained model will provide a framework for studying the cause of deviations of the brain age from chronological age in individuals with neuropathology, potentially leading to early biomarkers or a better mechanistic understanding of brain integrity in disease.

## Materials and methods

### Participants

Data were collected from 279 participants aged 5–81 years (116 males, 163 females), with a mean chronological age of  $31.0 \pm 21.3$  years, corresponding to eight studies with similar MRI protocols, which included an MRE scan and a high resolution

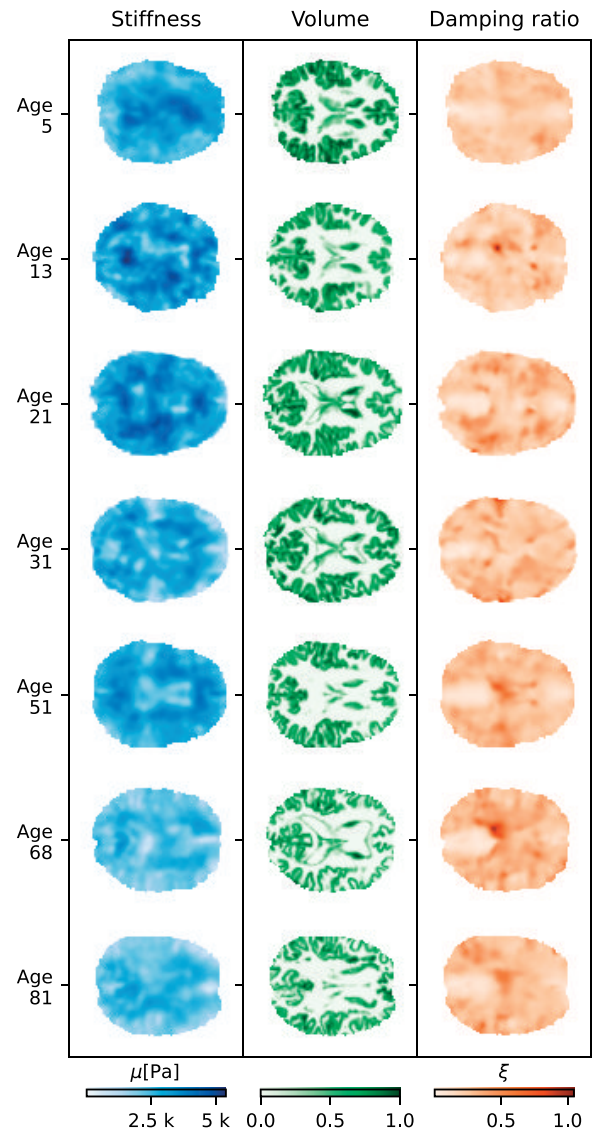


**Figure 1.** Stiffness, damping ratio, and volume map slices (axial with  $z = 28$ ) for cognitively normal subjects of different ages. Stiffness measurements (left) and volume measurements (middle) show decreases in the older subjects.

T1-weighted anatomical scan. Scans were performed at the University of Delaware (UD) with a Siemens 3 T Prisma MRI scanner or at the University of Illinois at Urbana-Champaign (UIUC) with a Siemens 3 T Trio MRI scanner. An overview of the participant demographics and imaging parameters for each study is shown in Table 1. Informed written consent was provided prior to scanning by all participants and by guardians of participants under the age of 18. All study protocols were approved by the Institutional Review Boards of the respective institutions. Data collected at UIUC was previously pooled and used to create a standard-space atlas of brain mechanical properties [42]. Additional data included in this work has been reported partially in previous publications [7, 19, 43–46]. Readers are referred to prior works for additional information.

### Imaging data and pre-processing

MRI data included a whole-brain, high-resolution T1-weighted magnetization-prepared rapid acquisition gradient echo (MPRAGE)

**Table 1.** Summary of study characteristics and data acquisition settings.

| Study                | $\mathcal{S}_1$ | $\mathcal{S}_2$ | $\mathcal{S}_3$ | $\mathcal{S}_4$ | $\mathcal{S}_5$ | $\mathcal{S}_6$ | $\mathcal{S}_7$ | $\mathcal{S}_8$ |
|----------------------|-----------------|-----------------|-----------------|-----------------|-----------------|-----------------|-----------------|-----------------|
| N                    | 9               | 29              | 61              | 19              | 22              | 53              | 76              | 10              |
| # M/F                | 1/8             | 1/28            | 27/34           | 12/7            | 14/8            | 23/30           | 34/42           | 4/6             |
| Age range (years)    | 20–60           | 18–32           | 18–35           | 12–15           | 5–8             | 14–73           | 23–81           | 12–14           |
| Site                 | UIUC            | UIUC            | UIUC            | UD              | UD              | UD              | UD              | UD              |
| Scanner model        | Trio            | Trio            | Trio            | Prisma          | Prisma          | Prisma          | Prisma          | Prisma          |
| Head Coil (channels) | 32              | 32              | 32              | 64              | 64              | 64              | 64              | 64              |
| <b>T1 MPRAGE</b>     |                 |                 |                 |                 |                 |                 |                 |                 |
| TE (ms)              | 2.32            | 2.32            | 2.32            | 2.32            | 2.32            | 2.32            | 2.32            | 2.32            |
| TR (ms)              | 1900            | 1900            | 1900            | 2300            | 2300            | 2300            | 2300            | 2300            |
| Resolution (mm)      | 0.9             | 0.9             | 0.9             | 0.9             | 0.9             | 0.9             | 0.9             | 0.9             |
| <b>MRE</b>           |                 |                 |                 |                 |                 |                 |                 |                 |
| Frequency (Hz)       | 50              | 50              | 50              | 50              | 50              | 50              | 50              | 50              |
| Sequence             | Spiral          | Spiral          | Spiral          | Spiral          | Spiral          | Spiral          | Spiral          | Spiral          |
| Resolution (mm)      | 1.6             | 2.0             | 1.6             | 1.5             | 1.5             | 1.5             | 1.25            | 1.5             |
| Number of slices     | 60              | 60              | 60              | 80              | 64              | 80              | 96              | 80              |

with 0.9 mm<sup>3</sup> isotropic resolution and a high-resolution MRE scan. All MRE data were collected using a pneumatic actuator pillow system (Resoundant, Rochester, MN) at 50 Hz vibration. MRE data acquisitions were taken using either the 3D multislabs, multishot spiral sequence [47] or the 3D multiband, multishot spiral sequence [48, 49], with resolutions ranging from 1.25 to 2.0 mm isotropic, and whole-brain coverage. Images were downsampled to 2.0 mm resolution prior to analysis. Each MRE scan had a corresponding field map of the same resolution and brain coverage, which was used during image reconstruction to minimize geometric distortion [50]. Displacement images from MRE were converted into maps of mechanical properties using the nonlinear inversion (NLI) algorithm [51], which returns estimates of the complex-valued shear modulus,  $G^* = G' + iG''$ , where  $G'$  is the storage modulus and  $G''$  is the loss modulus. Mechanical property measures of stiffness ( $\mu$ ) and damping ratio ( $\xi$ ) are calculated as  $\mu = \frac{2|G'|^2}{G' + |G'|}$  and  $\xi = \frac{G''}{2G'}$  [52, 53].

The high-resolution T1 image and MRE magnitude data were skull stripped using the Brain Extraction Tool (BET) in the FMRIB Software Library (FSL) [54]. The MRE images were registered to the corresponding T1-weighted anatomical image using FSL FLIRT [55], which allows for an affine linear transformation, and the transform was similarly applied to the individual mechanical property maps. The T1-weighted anatomical scan was registered to the standard space MNI152 2-mm template with dimensions 91 × 109 × 91 using a nonlinear registration with FSL FNIRT [56].

Volume maps were created from the high-resolution T1-weighted anatomical images using voxel-based morphometry (VBM) in FSL-VBM [57, 58]. Several previous studies have shown that VBM measures are sensitive to age-related changes to the brain [59–61]. In the VBM pipeline, the T1-weighted anatomical images were brain-extracted and grey matter was segmented using FSL FAST [62]. Data were then registered to the MNI152 standard space using the FNIRT non-linear registration. The resulting images per study are averaged, including flipping along the x-axis, to create a left-right symmetric, study-specific grey matter template. Then, all grey matter segmented images were non-linearly registered to this study-specific template. The grey matter images were then smoothed with an isotropic Gaussian kernel with  $\sigma = 2$  mm. The resulting images depict the morphometry of grey matter regions and are effectively voxel-wise maps of volumetric measures.

Prior to being input to the CNN, all mechanical property and volumetric maps were truncated in the axis z, which is composed of 91 slices. Specifically, slices 16–70 are considered to account

for the top and bottom slices being outside the imaging field-of-view for some subjects. After truncation, each brain map then had dimensions of 91 × 109 × 55. Maps of each type (stiffness, damping ratio, or volume) were separately standardized so that the mean of all voxels across the entire sample of subjects was 0 and the standard deviation was 1. Voxels outside of the brain tissue were set to 0.

## Dataset splits

Cross-validation is a standard technique for splitting data into folds in order to test the variability of models' prediction performance on multiple independent subsets of the data. Given that the dataset is composed of studies with slightly different data acquisition settings, with distinct age distributions per study (Table 1), there is the possibility for the model to identify spurious correlations in the data related to the acquisition parameters to predict the age. Thus, it is crucial to evaluate the ability of the brain-age predictions to generalize to not only held-out subjects but also held-out studies.

We performed a stratified strategy to create 5-folds  $\{\mathcal{D}_k\}_{k=1}^5$  for cross-validation from the eight studies  $\{\mathcal{S}_i\}_{i=1}^8$ , where  $\mathcal{D}_k$  and  $\mathcal{S}_i$  denote the set of subjects in the  $k$ th fold and the  $i$ th study, respectively. More specifically,  $\mathcal{S}_i = \{(\mathbf{x}_t, y_t) | t \in \{1, \dots, N_i\}\}$ , where  $\mathbf{x}_t \in \mathbb{R}^{91 \times 109 \times 55}$  is the brain image,  $y_t \in \mathbb{R}^+$  is the corresponding chronological age, and  $N_i \in \mathbb{N}$  is the total number of subjects in study  $\mathcal{S}_i$ . The five smaller studies  $\mathcal{S}_1$ ,  $\mathcal{S}_2$ ,  $\mathcal{S}_4$ ,  $\mathcal{S}_5$ , and  $\mathcal{S}_8$ , which each contain fewer than 50 subjects, were wholly allocated to folds 1, 2, 3, 4, 5, respectively. Subjects from the larger studies ( $\mathcal{S}_3$ ,  $\mathcal{S}_6$ , and  $\mathcal{S}_7$ ) were randomly sampled without replacement to complete the folds, such that each fold contains roughly 56 subjects (20% of the data set). Given these folds, cross-validation of the  $k$ th model used subjects in  $\mathcal{D}_k$  for testing after using the union of all the remaining folds (around 224 subjects) for model training and internal validation to select model hyperparameters. Figure 2 shows the age distributions for each of the resulting splits.

## CNN model architectures

We selected the ResNet Model [39] and Simple Fully Convolutional Network (SFCN) [40] as deep learning architectures as they show a strong performance when using voxel-based inputs [34]. Specifically, we implemented the ResNet-34 architecture with pre-activation Residual Units [63] and a regression head. The SFCN was mostly implemented as described in the original protocol [40], but the last head was modified for a regression head. The brain map(s) input is denoted  $\mathbf{x} \in \mathcal{X} \subset \mathbb{R}^{P \times 91 \times 109 \times 55}$ ,

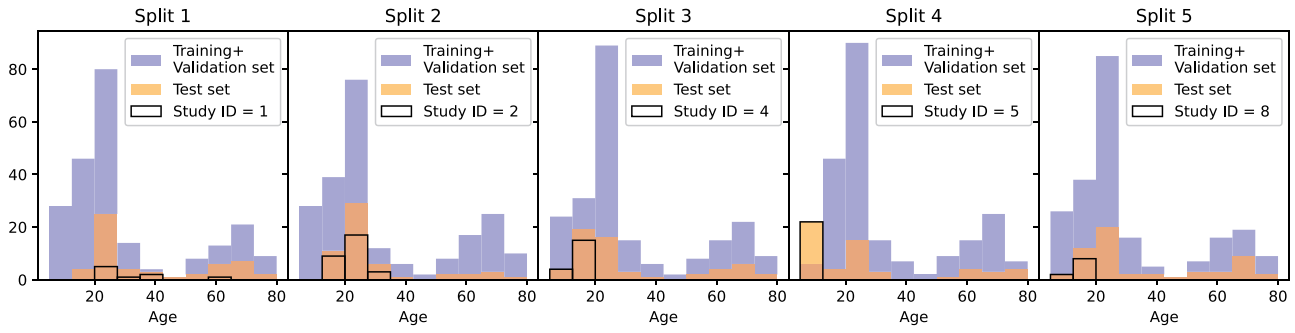


**Figure 2.** Age distributions for the training, validation, and test groups in each data split. These histograms show a similar age distribution in the training and validation sets across splits. However, due to the five smaller studies each wholly assigned to a single fold, the age distribution of test sets differ. The contribution of the five smaller studies to the age distribution of the fold is outlined in each split.

where the first dimension is  $P = 1$  if only a single modality is used and  $P > 1$  if multiple modalities are used. If the input was multi-modal, the architecture was repeated for each input and concatenated at the regression head. Complete code is available at [https://github.com/cesar-claros/MRE\\_MRI\\_BrainAge](https://github.com/cesar-claros/MRE_MRI_BrainAge).

### CNN model training and hyperparameter tuning

To form a prediction model for the  $k$ th fold, we optimized the model parameters  $\theta_k$  and selected the hyperparameters  $\phi_k$  that minimized the mean squared error (MSE) as the loss function, that is, we computed  $\theta_k^*, \phi_k^* = \operatorname{argmin}_{\theta_k, \phi_k} \mathbb{E}[(y - f_{\theta_k}(\mathbf{x}; \phi_k))^2]$ , where  $f_{\theta_k}: \mathcal{X} \rightarrow \hat{\mathcal{Y}}$  is the model trained using the  $k$ th split (all folds but the  $k$ th),  $\phi_k$  are the hyperparameters,  $y \in \mathcal{Y} \subset \mathbb{R}_+$  is the true target, and  $f_{\theta_k}(\mathbf{x}) = \hat{y} \in \hat{\mathcal{Y}} \subset \mathbb{R}_+$  is the predicted output. For both models, the optimization of the model parameters  $\theta$  used stochastic gradient descent with momentum and weight decay for a maximum of 100 epochs. Additionally, a learning rate scheduler reduced the learning rate by a factor of 10 if there was no loss reduction after 10 consecutive epochs and stopped training early if the loss did not decrease after 50 consecutive epochs. The hyperparameters consisted of the batch size  $B \in \{4, 8, 12, 16, 20\}$ , momentum  $\mu \in \{0.99, 0.9, 0.5\}$ , weight decay  $\lambda \in \{10, 1, 1e^{-1}, 1e^{-2}, 1e^{-3}\}$ , and learning rate  $\gamma \in [1e^{-5}, 1e^{-4}]$ . To optimize the hyperparameters  $\phi$ , we ran a hyperparameter search using the Tree-structured Parzen Estimator (TPE) [64] that iteratively selects a hyperparameter configuration based on performance of previous configurations. The best model configuration for each data split was selected based on the mean-squared (MSE) error loss in the validation set across 100 configurations, where the first 10 configurations were selected randomly and TPE selected the remaining 90.

### Baseline models

To compare the performance of the CNNs to more traditional statistical models, we employed two models as baselines: a linear regression model with ElasticNet regularization [65] and a RF model [66], which is a non-linear model formed as an ensemble of decision trees. These baselines cannot exploit the 3D arrangement of the brain maps and cannot operate directly on the vectorized brain maps due to their high number of voxels. Therefore, we tested a range of different methods for preprocessing inputs to these models, described in more detail below, and identified the method-model combination that resulted in the lowest MAE.

First, we considered summarizing the brain maps into ROIs through parcellation using functional and anatomical atlases. ROI-based feature extraction is widely used to obtain lower-

dimensional vectors suitable for model training [67–73]. However, the optimal choice of brain atlas can significantly impact the model’s ability to reveal or obscure brain-age associations [69]. To mitigate this, we trained models based on multiple anatomical and functional atlases, including those from NeuroParc [74] and NeuroVault [75]. The best-performing atlas was selected based on the validation sets’ MAE performance for each brain modality. For atlases lacking full brain coverage, complementary atlases were incorporated to ensure whole-brain representation, resulting in a complete feature set for training regression models.

We also considered unsupervised dimensionality reduction techniques that exploit the covariance among voxels across subjects. Specifically, we applied Principal Component Analysis (PCA) [76], Non-negative Matrix Factorization (NMF) [77], and Orthogonal Projective NMF (OPNMF) [78, 79]. Unsupervised dimensionality reduction techniques are multivariate approaches that capture the covariance among features. Previous research [71, 73, 80–85] suggests that dimensionality reduction techniques often outperform ROI-based approaches. In particular, NMF and OPNMF provide spatially compact features that have been shown to improve the prediction of brain-related traits. We optimized the number of components for each technique through validation set MAE in each data split.

Lastly, we considered multi-modal models that combine the best representation of each brain modality to train our baseline models. For combined modalities of ROI summarization, we concatenated the features generated by the best-performing atlas for each modality. The best atlas was determined by how frequently it was chosen across the five data splits. For dimensionality reduction, we followed a similar process where we concatenated the components that achieved the lowest MAE for each data split and modality, and then trained the model that performed the best in the validation set using this combined representation.

### CNN and baseline model performance metrics

Model quality was assessed using the root mean squared error  $\operatorname{RMSE} = \sqrt{\frac{1}{n} \sum_{i=1}^n (y_i - \hat{y}_i)^2}$ , the mean absolute error  $\operatorname{MAE} = \frac{1}{n} \sum_{i=1}^n |y_i - \hat{y}_i|$ , and the coefficient of determination  $R^2 = 1 - \frac{\sum_{i=1}^n (y_i - \hat{y}_i)^2}{\sum_{i=1}^n (y_i - \bar{y})^2}$ , where  $\bar{y} = \frac{1}{n} \sum_{i=1}^n y_i$  is the mean of the true ages and the true-prediction pairs  $(y_i, \hat{y}_i)$  are taken from the set  $\mathcal{T}$ , either  $\mathcal{T}_k = \{(y, f_{\theta_k}(\mathbf{x})) | (\mathbf{x}, y) \in \mathcal{D}_k\}$  for the  $k$ th fold or  $\mathcal{T}^{\text{all}} = \cup_{k=1}^5 \mathcal{T}_k$  for all folds.



## Statistical analysis of CNN performance

Wilcoxon signed-rank tests were used to test for significant differences in model performance for different sets of brain map modalities. Given two models, based on the same architecture, with modality sets A and B, respectively, the null hypothesis evaluated if the population median  $m$  of paired differences  $d_i = |e_i^A| - |e_i^B|$  is 0, where  $|e_i^C| = |y_i - \hat{y}_i|$  is the absolute error for the  $i$ th subject made by a model trained for modality set C,  $(y_i, \hat{y}_i) \in \mathcal{T}^{\text{all}}$ . If the null hypothesis  $H_0 : m = 0$  held, then the performances of models optimized for two modality sets cannot be distinguished. Given that we tested multiple hypotheses, we applied the Holm–Bonferroni method to evaluate statistical significance with correction for multiple comparisons. Two-sided tests were conducted between the models with unimodal input, and one-sided tests were conducted to compare a multimodal model with a unimodal model.

## CNN prediction correlation and ensembled predictions

Models with uncorrelated errors indicate independent sources of noise; thus, models with correlated errors are expected when the model input is shared. To investigate how prediction errors are correlated between different models with the same or different input, we computed the Pearson correlation for every pair of models. Ultimately, this could provide insights into whether stiffness and volume contain similar sources of noise, which would suggest that they are influenced by the same underlying factors.

Pooling model predictions, also known as ensembling, is known to improve performance [86, 87], as an ensemble average prediction reduces the error from independent noise sources. The multimodal model architecture we used combines features extracted from each of the input maps at the regression head, which allows the feature extraction to specialize for each given the other. However, if the input maps are truly complementary, then the extracted features will not depend on each other. In this case, unimodal models’ predictions could be directly combined (by averaging) to improve prediction performance. To test this, we evaluated predictions formed by averaging pairs of model predictions.

## CNN interpretation via salient activation maps

The spatial maps of the most salient activations in deep learning models provide a visual way of understanding which brain regions are driving model predictions [88–90]. Applied to unregistered images, these salient activation maps, or saliency maps, are typically visualized for each instance separately. However, since the brain maps are registered to a standard template, we computed Regression Activation Maps (RAMs) [41] for each subject in an age range and visualize the averages of the saliency maps for different age ranges. Individual RAMs are a weighted sum of the feature activation maps at the last convolutional layer of a model, where the weights are based on the connections between the feature map and the output. Importantly, the convolutional layer’s spatial dimensions correspond to subsampled versions of the input data.

Mathematically, the input  $\mathbf{x} \in \mathcal{X} \subseteq \mathbb{R}_+^{P \times W \times H \times D}$  is passed to a trained model  $f : \mathcal{X} \rightarrow \mathcal{Y} \subseteq \mathbb{R}_+$ , which acts as the composition of two functions  $f(\mathbf{x}) = g(h(\mathbf{x})) : h : \mathcal{X} \rightarrow \mathcal{T} \subseteq \mathbb{R}^{P \times C \times D_1 \times D_2 \times D_3}$  is the mapping between the input and the convolutional layer’s activations and  $g : \mathcal{T} \rightarrow \mathcal{Y}$  is the mapping from the convolutional layer’s activations to the target domain. For unimodal models  $P = 1$ , but for multimodal models, namely  $P = 2$ , we analyzed the salience of the activations of the inputs separately, which is possible since they are concatenated at the prediction head. The 3D saliency

map  $L_{i,p}^{\text{RAM}} \in \mathbb{R}^{D_1 \times D_2 \times D_3}$ , which highlights the regions predictive of the age of subject  $i$  for input  $p$ , is computed as

$$L^{\text{RAM}}(\mathbf{x}_{i,p}) = \sum_{c=1}^C [\alpha(\mathbf{x}_i)]_{p,c} [h(\mathbf{x}_i)]_{p,c}, \quad (1)$$

where  $[h(\mathbf{x}_i)]_{p,c}$  is the  $c$ th feature map in the convolutional layer’s output to input  $p$ , the weight associated to the  $c$ th feature map is  $[\alpha(\mathbf{x}_i)]_{p,c} = \frac{1}{Z} \sum_{d_1} \sum_{d_2} \sum_{d_3} \frac{\partial \hat{y}}{\partial [h(\mathbf{x}_i)]_{p,c,d_1,d_2,d_3}}$ , and  $Z = D_1 \cdot D_2 \cdot D_3$  is the normalization factor. It should be noted that the voxels in the saliency map can have positive or negative values, which indicate that some voxels will highlight regions that contribute to the age prediction being higher or lower, respectively. We upsampled the saliency map  $L^{\text{RAM}}(\mathbf{x}_{i,p})$  to the same dimensions of the input for visualization purposes. The upsampled version is denoted by  $L^{\text{RAM}(\uparrow)}(\mathbf{x}_{i,p})$ .

Considering that the participants in our studies ranged in age from 5 to 81, we visualized brain regions that contribute to the brain age prediction in different age ranges by averaging the saliency maps for participants that belong to a given age bin across all folds. Note that even though we trained a separate model for each fold, we averaged the saliency maps of individuals from different trained models of the same architecture. More concretely, from the age bin  $\mathcal{B}_t = [a_t, b_t]$  with limits  $a_t < b_t$ , we averaged the saliency maps for input  $p$  over the set of subjects pooling across folds  $\mathcal{R}_t = \{\mathbf{x}_i | (\mathbf{x}_i, y_i) \in \mathcal{D}_k^{\text{est}}, y_i \in \mathcal{B}_t, k \in \{1, \dots, 5\}\}$ , yielding  $\bar{L}_{\mathcal{R}_t,p}^{\text{RAM}(\uparrow)} = \frac{1}{n} \sum_{i=1}^n L^{\text{RAM}(\uparrow)}(\mathbf{x}_{i,p})$ ,  $\forall \mathbf{x}_i \in \mathcal{R}_t$  and  $n = \text{card}(\mathcal{R}_t)$ . The binned aggregations highlight the spatial locations of features consistently used in a range bin. Additionally, we computed the Spearman correlation  $r_s$  for each voxel of the saliency map to the true age to identify regions whose activations have a monotonic relationship with age.

To concretely associate the saliency maps with specific brain regions, we used the Harvard-Oxford atlas [91–94] to parcellate the maps into 48 cortical brain regions. For each region, we computed the proportion of voxels (out of the total number of voxels in the region) where strong saliency is present. Strong saliency, in our case, is defined as saliency magnitudes in the averaged saliency map  $\bar{L}_{\mathcal{R}_t,p}^{\text{RAM}(\uparrow)}$  that are greater than their 90th percentile. Strong saliencies were computed for each age bin  $\mathcal{B}_t$  for a given input  $p$  and model architecture.

## Results

### Performance of CNN and baseline models

Table 2 details the brain age prediction performance for various brain map measurements (stiffness, volume, damping ratio, and

**Table 2.** Performance metrics for model-input pairs.

| Model         | Input                 | RMSE       | R <sup>2</sup> | MAE        |
|---------------|-----------------------|------------|----------------|------------|
| ResNet        | Stiffness             | 7.7        | 0.87           | 5.8        |
|               | Volume                | 7.8        | 0.86           | 5.4        |
|               | Damping Ratio         | 13.4       | 0.60           | 9.7        |
|               | [Stiffness, Volume]   | <b>6.6</b> | <b>0.90</b>    | <b>4.8</b> |
| SFCN          | Stiffness             | 8.3        | 0.84           | 6.0        |
|               | Volume                | 9.0        | 0.82           | 6.5        |
|               | Damping Ratio         | 10.7       | 0.74           | 8.3        |
|               | [Stiffness, Volume]   | <b>7.8</b> | <b>0.86</b>    | <b>5.8</b> |
| RF (Baseline) | Stiffness (OPNMF)     | 8.0        | 0.84           | 5.6        |
|               | Volume (NMF)          | 10.0       | 0.76           | 7.0        |
|               | Damping Ratio (OPNMF) | 12.00      | 0.63           | 8.3        |
|               | [Stiffness, Volume]   | <b>7.6</b> | <b>0.86</b>    | <b>5.6</b> |

Bolded numbers highlight the input that produced the best performance for each model. For both deep neural network architectures and baseline, using the multimodal input ‘[Stiffness-Volume]’ produced the best results.

a combination of stiffness and volume) for the deep neural networks and the best baseline model, which was chosen from RF and ElasticNet models that used either atlas-based ROI summarization or dimensionality reduction techniques (PCA, NMF, OPNMF). The best baseline model across all possible inputs was the RF model; for stiffness and damping ratio, applying dimensionality reduction using OPNMF performed the best, and for volume, applying dimensionality reduction using NMF performed the best. Overall, the multimodal models that combined stiffness and volume achieved the lowest MAE and RMSE values and highest  $R^2$  values across both deep neural network architectures and the baseline approaches: ResNet achieve an MAE of 4.8 and an  $R^2$  of 0.90, SFCN achieve an MAE of 5.8 and an  $R^2$  of 0.86, and as the best baseline RF achieved an MAE of 5.6 and  $R^2$  of 0.86. Using stiffness had the next highest  $R^2$  values (0.87, 0.84, and 0.84 for ResNet, SFCN, and RF, respectively). There was a larger gap in performance between the deep neural networks and baseline when using volume alone, with  $R^2$  values of 0.86, 0.84, and 0.76, for ResNet, SFCN, and RF, respectively. Finally, models using damping ratio had the lowest performance and thus are excluded from further analyses.

In [Supplementary Appendix, Figs A2a and A2b](#) show the correspondence between the true age and predictions for each of the splits and input types for SFCN and ResNet models. The baseline results are further expanded in [Supplementary Appendices B and C](#) and detailed in [Tables A1–A4](#).

### Statistical significance of CNN performance

We conducted paired Wilcoxon rank-sign tests between the absolute error of the test set predictions across all subjects for the deep neural network models of the same architecture but trained on different inputs ( $l = 6$  different pairs of models). Two-tailed tests are used between unimodal models, and one-tailed tests are used for testing whether multimodal models have lower absolute errors than unimodal models. We selected a significance level of  $\alpha = 0.1$ , and applied the Holm-Bonferroni procedure to account for multiple tests. [Table 3](#) encapsulates the results of the tests. For both architectures, the multimodal model that combines stiffness and volume maps outperforms a unimodal volume-only model. Additionally, for the ResNet architecture, the multimodal model outperforms the unimodal stiffness-only model.

### Correlation of CNN predictions for different modalities

To investigate whether prediction errors are correlated between different deep neural network models with the same or different input, we computed the Pearson correlation for every pair and report the resulting matrix in [Fig. 3](#). Models with the same input but different architecture are the most correlated. An exception is the SFCN multimodal model that is correlated with the SFCN unimodal models. Models using damping ratio are the least correlated. Notably, the unimodal models for stiffness and volume are relatively uncorrelated (0.32 for ResNet and 0.52 for SFCN).

### CNN prediction pooling improves performance

We hypothesized that pooling the predictions from the volume and stiffness deep neural network models would lower the prediction error. The relatively low correlation between prediction errors for the ResNet volume and stiffness models suggests that these measures may be independent and provides some support for this hypothesis. To further test this hypothesis, we reported the MAEs of the predictions of the pooled models (excluding

**Table 3.** Statistical significance of differences in model performance.

| Input               |           | Model         |               |
|---------------------|-----------|---------------|---------------|
| A                   | B         | ResNet        | SFCN          |
| Stiffness           | Volume    | 0.1777        | 0.0980        |
| [Stiffness, Volume] | Stiffness | <b>0.0002</b> | 0.2682        |
| [Stiffness, Volume] | Volume    | <b>0.0137</b> | <b>0.0109</b> |

Bolded P-values denote significant difference in the absolute errors between models with input A versus input B.

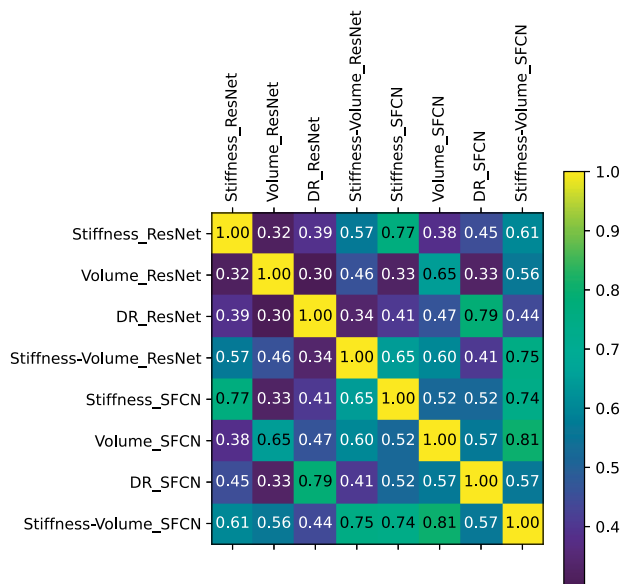


**Figure 3.** Correlation of brain age predictions errors between pairs of models. Models with the same input, but different architecture are the most correlated (besides the SFCN multimodal model that is correlated with the SFCN unimodal models).

damping ratio models) and showed that the errors of the pooled predictions (off-diagonal entries) are generally lower than the single model (diagonal entries) ([Fig. 4](#)). For ResNet, pooled and multimodal models both yield an MAE of 4.8 years, which is 0.6 years better than the volume-only model and 1 year better than the stiffness-only model. For SFCN, the pooled model yields an MAE of 5.4 years, which is 1.1 years better than the volume-only model, 0.6 years better than the stiffness-only model, and 0.4 years better than the multimodal model. Together, these results confirm our hypothesis that pooling predictions from stiffness and volume deep neural network models lowers the prediction error and suggests that stiffness and volume are complementary measures.

The two lowest MAEs are achieved by pooling the multimodal ResNet model with unimodal ResNet models: pooling the stiffness-volume model with the stiffness-only model achieves an MAE error of 4.6 years and pooling the stiffness-volume model with the volume-only achieves an MAE of 4.4 years. This means that while the multimodal model is able to extract information from both, it may be overfitting to just one modality and missing valuable information captured in the unimodal predictions.

### CNN model interpretation through saliency maps

We computed saliency maps via RAM [41] to compare and contrast the average saliency for predicting age across different

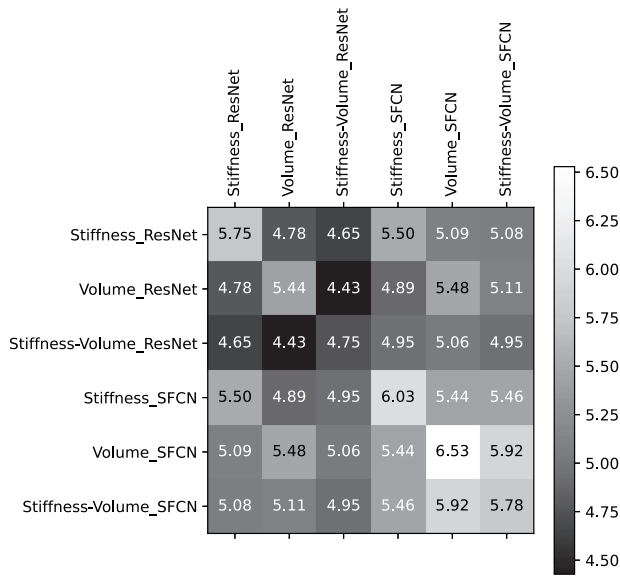


**Figure 4.** Mean absolute error for pooling between pairs of models (lower is better). Original model performance is along the diagonal. Pooling generally improves performance.

inputs and architectures. Figure 5 show the axial view of the ResNet model activations overlaid on top of an MNI152 brain template, and Supplementary Appendix Fig. A3 shows the same for the SFCN.

Once the saliency maps were computed for each input, we used the Harvard-Oxford parcellation to identify relevant brain regions used by the models. In the Supplementary Appendix, Tables A6–A9 detail the proportions of strong saliency for the models we considered in this analysis, and Fig. A4 visualizes the saliency across bin ages and ROIs. Overall, we observe that the strong saliency derived from the both stiffness and volume input maps overlap very little. In particular, volume measurements in brain regions 7 and 26 (precentral gyrus and juxtapositional lobule cortex, respectively) produce consistently strong saliency for both models. For stiffness measurements, brain regions 1, 3, 4, and 28 (frontal pole, superior frontal gyrus, middle frontal gyrus, and paracingulate gyrus) appear to be important in the last two age ranges (50–65 years and 65–81 years).

## Discussion

### On the predictive power of structural and mechanical brain measurements

We sought to investigate the performance of models that use measurements of the brain’s mechanical properties (stiffness and damping ratio) for predicting brain age with or without brain volume measurements. Brain volume is a well-studied structural measure for understanding brain age and has previously been found to predict chronological age with a high level of accuracy [34]. Over the past decade, MRE measures of tissue stiffness and damping ratio have revealed notable aging-related changes [12, 13, 16], with tissue softening occurring during development presumably due to synaptic pruning, and softening occurring across later life due to age-related neurodegeneration. However, the use of whole-brain maps of mechanical properties to predict age had not been investigated.

The results from both baseline models and the deep neural network models confirm that stiffness measurements match or exceed cortical volume measurements in their utility for

predicting brain age. Furthermore, stiffness and volume maps provide complementary information, which significantly enhances predictive accuracy when combined in a multimodal approach. Both deep learning models and the baseline RF model that use stiffness and volume together achieve higher performance than the models that use only a single measurement type. Our finding that stiffness and volume are complementary measures for predicting brain age echoes previous findings by Hiscox *et al.* [4], which shows that stiffness measurements carry age-related information even after accounting for the volumes of the ROIs. This synergy between stiffness and volume reflects the distinct yet complementary aspects of brain structure and tissue integrity captured by each modality. While volume reflects macroscale structural changes, stiffness offers insights into microstructural health, and together they provide a more comprehensive picture of brain aging. This highlights the importance of leveraging multiple brain imaging modalities to improve the accuracy of age prediction models.

In contrast, the models that used maps of tissue damping ratio were not as accurate. Stiffness and damping ratio are independent measures, and it is expected that damping ratio reflects an organizational aspect of the tissue while stiffness reflects a compositional aspect of the tissue [95]. Differences in brain damping ratio with age are less commonly reported [11], but have been observed in brain maturation [18, 19] and in aging [13]. Hiscox *et al.* [4] reported a 21% difference in hippocampal damping ratio between younger and older adults, but other brain regions did not significantly differ in damping ratio. Our experiments showed that damping ratio as the only input is less accurate than volume and stiffness maps, but still correlates with age with an  $R^2$  value in range of 0.60–0.74. This may be because damping ratio reflects more individual differences in tissue structure. For instance, damping ratio of specific brain regions has been related to differences in cognitive function across several different types of behavioral assessments [11, 96, 97]. Thus, the features of damping ratio maps are not as strongly influenced by age, leading to heightened error, especially from a small training set.

### On the choice of deep over shallow networks for predicting brain age

In our study, we leveraged deep CNNs, namely ResNet and SFCN, to model high-dimensional brain imaging data (MRI and MRE) in a healthy population. While the “no free lunch” theorems [98–100] suggests that no single model class is universally superior, domain-specific inductive biases—like those present in deep networks—can provide a distinct advantage in specific tasks involving spatial patterns. Practically, the relationship modeled here is very similar to those in various medical imaging applications [101–105]. In particular, deep CNNs have previously been applied to whole-brain neuroimaging data for image preprocessing, diagnostic classification, regression, disease prediction, and disease and aging characterization [106–114]. CNNs are particularly advantageous in whole-brain neuroimaging as they can extract spatial patterns without relying on spatial priors or pre-defined structures such as ROIs. In contrast to ROI-based analysis, CNNs can examine the entirety of the input image without breaking the spatial information, allowing them to detect subtle changes with age, such as those that occur with different rates or spatial extent and that vary at different stages of aging. This flexibility is crucial given the heterogeneous nature of brain aging, which varies temporally and spatially, and encompasses a wide range of what is considered ‘healthy’ variation [115–119].

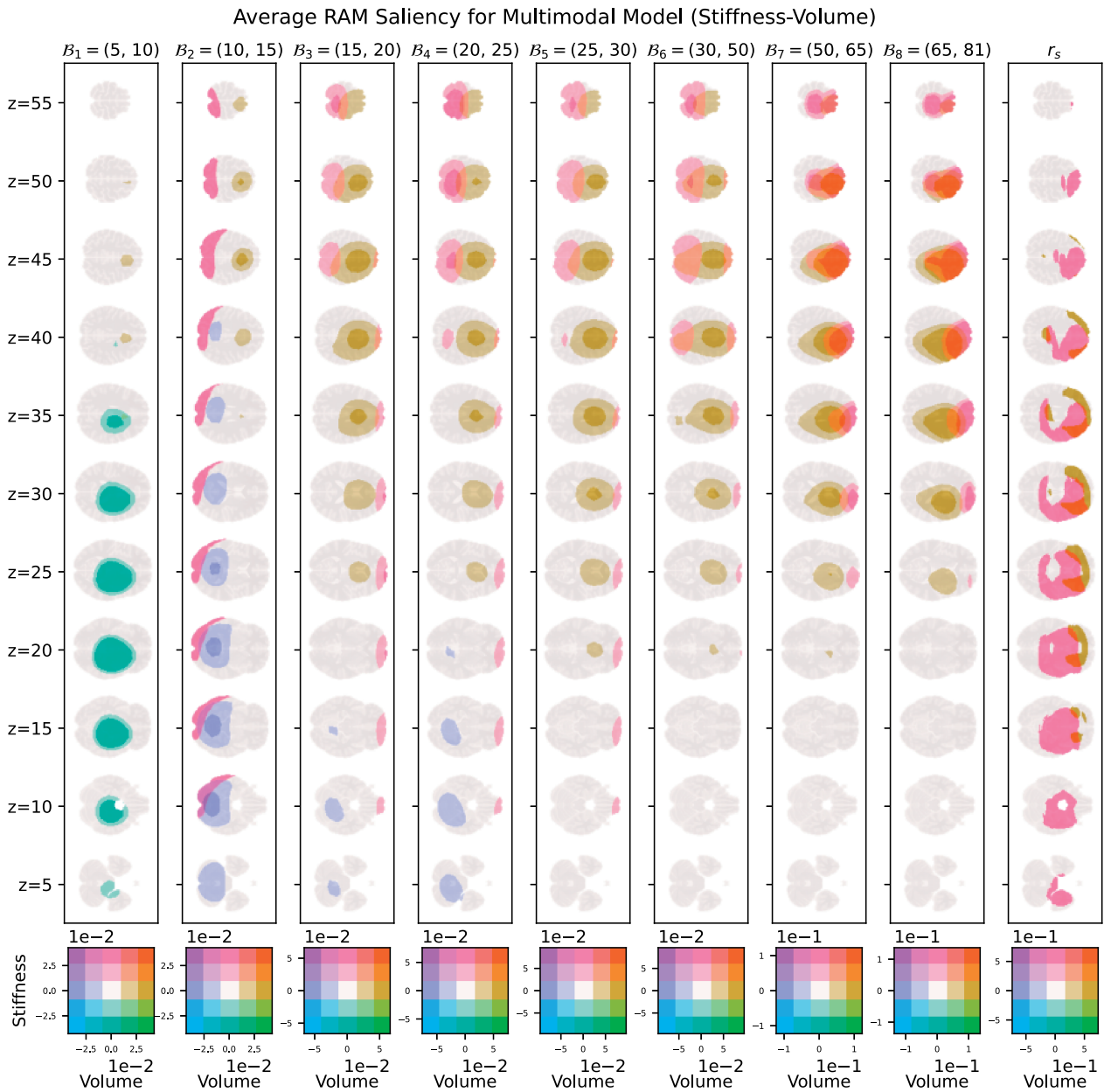


**Figure 5.** Multimodal ResNet model activations. This plot shows axial views of averaged RAMs for different age bins using the trained multimodal ResNet model overlaid on slices of an MNI152 skullstripped T1 brain template with the front facing the right and superior slice ( $z = 55$ ) at the top and inferior ( $z = 5$ ) at the bottom. Each column corresponds to the averaged RAM for participants who belong to age bin  $B_i$ . The last column shows the Spearman correlation of each voxel’s saliency to the chronological age.

Theoretical support for using a deep CNN like ResNet, despite the limitations of sample size (approximately 224 subjects per split in our study), is found in the architecture’s inherent advantages over shallow networks. For example, deep CNNs efficiently model spatial hierarchies through weight sharing and locality, greatly reducing the number of parameters compared to fully connected shallow networks [120]. In contrast, the initial layer of a fully-connected shallow network has parameters on the order of the number of voxels. Training this large number of weights in the initial layer will lead to trivial overfitting [105], without strong regularization and randomization methods like drop-out.

Specifically, CNNs efficiently extract information from spatial patterns in a hierarchical manner due to inductive biases

inherent in CNNs, namely, weight sharing and locality [121], and for deep CNNs like ResNet, the complexity of functional families grows more rapidly with additional layers through the composition of functions. In a convolution layer, the weights defining each filter are applied across space, greatly reducing the number of parameters. Furthermore, the use of small filters ensures spatially local features, which capture finer-grain structures in MRI and MRE data critical for accurate age prediction. A spatial hierarchy of these local features, necessary to capture long-range correlations, are created by CNN-specific operations like downsampling and multichanneling [121]. Downsampling expands the receptive field exponentially, making it possible to learn long-range dependencies with fewer layers. Multichanneling



supports storing information across reduced spatial dimensions, preserving essential features throughout the network's layers. Furthermore, compositionality is enhanced by ResNet's skip connections, which ensure the functional family realized by deeper networks subsumes shallower networks [122]. The skip connections enable efficient gradient propagation, reducing the risk of vanishing gradients and enabling smoother training convergence. Overall, deep CNNs provide a smooth optimization landscape, enhancing the likelihood of achieving a near-global minimum, while shallow networks often face rugged loss surfaces, which can trap the optimizer in suboptimal minima. The synergy between downsampling, multichanneling, and residual connections in deep CNNs is fundamental to architectures like ResNet, which we used in our experiments to achieve superior performance (4.8 MAE).

### On the interpretability of deep neural network predictions

Beyond the performance quantification, the saliency maps of each model revealed which brain regions were most implicated in predicting age. One noteworthy cluster encompassed the supplemental motor cortex, subcallosal cortex, paracingulate gyrus, and cingulate gyrus. Both the ResNet and the SFCN showed volumetric changes in these regions across the entire lifespan, with stiffness contributing to age predictions more prominently in later stages of life. These regions are in the medial frontal lobe and extend into the limbic system, and they play a central role in motor planning, emotional regulation, decision-making, and cognitive control [123]. The changing natures of these functions across the life span is well documented, making it easily understandable why structure of these regions contribute most to predictions of age [124, 125].

Likewise, we found that frontal lobe volume played a large role in age determination across the lifespan. This was particularly true of the superior frontal gyrus. Interestingly, in all models, only volume was notable predictor in earlier life, while stiffness became a more dominant factor from age 50 onward. This aligns with research on the developmental and degenerative trajectory of the frontal lobe, where volume loss begins in early life with the phenomenon of synaptic pruning [126] and continues into later life with neurodegeneration [127], while age-related stiffness change in this region is stronger in older age than early life [16, 19].

Notably, subcortical gray matter structures were influential in predicting age in children ages 5–10 but became less relevant beyond childhood. These structures, such as the thalamus and caudate, are essential in early brain development as they support fundamental processes like motor control, memory, and emotional regulation [128]. Volumetric changes to these regions occur mainly before age 5 and slow rapidly thereafter [129], but stiffness continues to mature across this time frame, likely because stiffness reflects microstructural organization, and volume reflects macroscale changes, and the later occurs prior to our window of study [19]. Finally, the ResNet model highlighted parietal lobe regions, such as the supramarginal and angular gyri, as important for age prediction. The parietal lobe is necessary for integrating sensory information and cognitive functions, which decline with age [130].

### On the associations of mechanical measurements and aging

The specific mechanism that causes brain stiffness to be highly sensitive to age-related changes in brain tissue integrity is an

area of ongoing research. It is well established that large scale structural brain changes occur across the lifespan, which in turn are likely to manifest as brain mechanical properties. During development, synaptic pruning of neural connections can cause a decline in grey matter volume [131], which occurs while myelination in the brain is increasing [132]. Interestingly, it has been recently reported that brain stiffness appears to decrease from childhood to early adulthood [19]. During normal adult aging, the brain undergoes a variety of degenerative changes, including decreases in the density of neurons, breakdown of myelin integrity, and the appearance of white matter lesions [133–135]. The impact of many of these microstructural effects on brain stiffness has been studied through preclinical MRE of animal disease models, where a breakdown or loss of tissue components results in softening [136–138]. This is consistent with age-related softening seen in the human brain, with different regions of the brain having different rates of softening likely reflecting different microstructural degradation of those regions [12].

Age-related softening can be exacerbated by neurological disorders. The purpose of brain age prediction is to build a framework for using whole brain maps of mechanical properties to better understand neurodegeneration through deviations in brain age from chronological age. Past work has demonstrated that MRE is very sensitive to tissue changes in a number of neurological conditions. For instance, stiffness has been shown to be sensitive to demyelination caused by multiple sclerosis (MS); one study found a 13% decrease in cerebral viscoelasticity in MS patients compared to healthy volunteers [10]. Stiffness has also been shown to be sensitive to changes caused by Parkinson's disease, including a significant reduction in lentiform nucleus stiffness between patients and healthy, age-matched controls [9]. Alzheimer's disease has been most studied with MRE, and studies have shown lower stiffness in regions particularly affected by the disease [6, 8, 139, 140]. Recent studies have shown that stiffness of specific brain regions can serve as effective biomarkers for differentiating between Alzheimer's and other forms of dementia [141, 142]. This heightened softening in disease in patterns reflecting the distribution of pathology in the brain point to the utility of using brain MRE metrics to predict brain age in neurodegenerative conditions including Alzheimer's disease and Parkinson's disease. We expect that the sensitivity of MRE, combined with the spatial pattern learning capabilities of machine learning, allow us to characterize neurodegenerative pathology even in subtle conditions like mild cognitive impairment. As the field of brain MRE grows, we hope to further expand this work to describe the degree of severity of neurodevelopmental delays like autism, fetal alcohol syndrome, and other general intellectual disabilities, by characterizing brain age as different from chronological age, ultimately providing an accessible metric that is representative of condition severity.

### Limitations

Data for our experiments were combined from multiple studies with slightly different imaging protocols and scanner hardware. Some of the studies had different MRE image resolutions, and even though the data are all registered to a standard 2 mm resolution template, differences in the imagery may remain. However, Hiscox *et al.* [42] took a similar approach in pooling data between multiple studies and sites, including those with different resolutions, and still observed consistent regional characteristics in brain properties across all subjects regardless of slight differences in specific acquisition details.

There is also an uneven distribution of age in some of the study datasets that were pooled for this project. Given that most of the studies were concentrated around certain ages and that the studies had different acquisition parameters, the model could have used patterns related to the acquisition parameters to predict brain age. To robustly evaluate whether this was occurring, we formed folds that held out studies and assessed the ability of the model to generalize to new studies not seen during training. Additionally, since the overall subject age distribution skewed towards younger adults and children, it may have been difficult for the model to learn the specific patterns of aging seen in older adults that are not strongly reflected in younger people. As the field of brain MRE expands, new models should be retrained with larger datasets to form even more robust predictions of brain age.

While the deep learning models used in this study can learn both intra-region and inter-region relationships in brain maps, their interpretation is not trivial. The saliency-based approach [41] we adopted is a step towards understanding these models, which can be combined with standard atlases to provide interpretation of brain regions. However, further analysis to better understand the changes in salient regions is necessary. We acknowledge that selection of a framework can have a large effect on the interpretation of results. While we have focused on ResNet as a deep convolutional neural network, which is theoretically justified and well-motivated based on success on other similar tasks, it is possible that a shallower network or other architecture with appropriate training could provide an equally, or better, performing model. Future work is needed to examine the advantages and disadvantages of deep and shallow networks for age prediction with brain mechanical property images.

While not examined in this study, the interpretation of the baseline ROI-based models is arguably easier in terms of the relevancy of the predefined regions. However, even if they are more interpretable, ROI-based summarization loses intra-region variation present in the images, which can result in lower model performance. This is particularly problematic when working with MRE data since stiffness is not homogeneous across brain regions [42, 143], and thus averaging stiffness values within a region can also lead to a loss of information. In contrast, unsupervised dimensionality reduction techniques, in particular, non-negative matrix factorization, yield lower-dimensional features without predefined ROIs that can be still be interpreted by the spatial extent of underlying factor. However, even though these features may be understandable, accurate predictions were only achieved with the non-linear Random Forest models, which combine these features in an ensemble of decision trees, creating difficulties in direct interpretation. Thus, post-hoc model interpretation would still be necessary to understand how a non-linear model relates the features corresponding to these spatial patterns to brain age.

## Conclusion

This is the first study to use deep learning models to predict brain age from whole-brain MRE measures of brain stiffness. We found that the models using brain stiffness maps performed on par or better than volume maps and the combination of brain stiffness and volume maps give a better prediction accuracy than volume maps individually. The findings of this study suggest that MRE measures provide additional information about the brain maturation and tissue degradation process which complement structural imaging metrics for brain age prediction. Given the high sensitivity of brain stiffness to age, future research should

consider adding mechanical property maps to brain age prediction models. This will become more feasible as more sites collect MRE and in larger sample sizes.

## Author contributions

Claudio Cesar Claros-Olivares (Formal analysis, Investigation, Methodology, Writing—original draft), Rebecca G. Clements (Conceptualization, Data curation, Investigation, Writing—original draft), Grace McIlvain (Conceptualization, Data curation, Writing—review & editing), Curtis L. Johnson (Funding acquisition, Project administration, Writing—review & editing), and Austin J. Brockmeier (Formal analysis, Methodology, Project administration, Writing—review & editing).

## Supplementary data

Supplementary data is available at *Biology Methods and Protocols* online.

*Conflict of interest statement.* None declared.

## Funding

This work was supported in part by grants from the National Institutes of Health: R01-AG05885, R01-EB027577, U01-NS112120, and the Delaware Community Foundation Boerger Fund. This research was supported in part using Information Technologies (IT) resources at University of Delaware.

## Data availability

Code is available at [https://github.com/cesar-claros/MRE\\_MRI\\_BrainAge](https://github.com/cesar-claros/MRE_MRI_BrainAge). Data from studies 1, 2, and 3 is available at <https://github.com/mechneurolab/MRE134> [42]. Data from study 6 is available at <https://nitrc.org/projects/bbir> [46]. Data from other studies is available via formal data sharing agreement.

## References

1. Betzel RF, Byrge L, He Y et al. Changes in structural and functional connectivity among resting-state networks across the human lifespan. *NeuroImage* 2014;**102 Pt 2**:345–57.
2. Freitas C, Perez J, Knobel M et al. Changes in cortical plasticity across the lifespan. *Front Aging Neurosci* 2011;**3**:5–8.
3. Takao H, Hayashi N, Ohtomo K. A longitudinal study of brain volume changes in normal aging. *Eur J Radiol* 2012;**81**:2801–4.
4. Hiscox LV, Johnson CL, McGarry MDJ et al. High-resolution magnetic resonance elastography reveals differences in sub-cortical gray matter viscoelasticity between young and healthy older adults. *Neurobiol Aging* 2018;**65**:158–67.
5. Johnson CL, Telzer EH. Magnetic resonance elastography for examining developmental changes in the mechanical properties of the brain. *Dev Cogn Neurosci* 2018;**33**:176–81.
6. Murphy MC, Huston J, Jack CR et al. Decreased brain stiffness in Alzheimer's disease determined by magnetic resonance elastography. *J Magn Reson Imaging* 2011;**34**:494–8.
7. Delgado PL, Hiscox LV, McIlvain G et al. Hippocampal subfield viscoelasticity in amnesic mild cognitive impairment evaluated with mr elastography. *Neuroimage Clin* 2023;**37**:103327.
8. Hiscox LV, Johnson CL, McGarry MDJ et al. Mechanical property alterations across the cerebral cortex due to Alzheimer's disease. *Brain Commun* 2020;**2**:fzcz049.

- [9]. Lipp A, Trbojevic R, Paul F et al. Cerebral magnetic resonance elastography in supranuclear palsy and idiopathic Parkinson's disease. *Neuroimage Clin* 2013;**3**:381–7.
- [10]. Wuerfel J, Paul F, Beierbach B et al. Mr-elastography reveals degradation of tissue integrity in multiple sclerosis. *NeuroImage* 2010;**49**:2520–5.
- [11]. Hiscox LV, Schwarb H, McGarry MDJ, Johnson CL. Aging brain mechanics: progress and promise of magnetic resonance elastography. *NeuroImage* 2021;**232**:117889.
- [12]. Arani A, Murphy MC, Glaser KJ et al. Measuring the effects of aging and sex on regional brain stiffness with MR elastography in healthy older adults. *NeuroImage* 2015;**111**:59–64.
- [13]. Delgorio PL, Hiscox LV, Daugherty AM et al. Effect of aging on the viscoelastic properties of hippocampal subfields assessed with high-resolution MR elastography. *Cereb Cortex* 2021;**31**:2799–811.
- [14]. Kalra P, Raterman B, Mo X, Kolipaka A. Magnetic resonance elastography of brain: comparison between anisotropic and isotropic stiffness and its correlation to age. *Magn Reson Med* 2019;**82**:671–9.
- [15]. Lv H, Kurt M, Zeng N et al. Mr elastography frequency-dependent and independent parameters demonstrate accelerated decrease of brain stiffness in elder subjects. *Eur Radiol* 2020;**30**:6614–23.
- [16]. Sack I, Streitberger KJ, Krefting D et al. The influence of physiological aging and atrophy on brain viscoelastic properties in humans. *Plos ONE* 2011;**6**:e23451.
- [17]. Takamura T, Motosugi U, Sasaki Y et al. Influence of age on global and regional brain stiffness in young and middle-aged adults. *J Magn Reson Imaging* 2020;**51**:727–33.
- [18]. McIlvain G, Schwarb H, Cohen NJ et al. Mechanical properties of the in vivo adolescent human brain. *Dev Cogn Neurosci* 2018;**34**:27–33.
- [19]. McIlvain G, Schneider JM, Matyi MA et al. Mapping brain mechanical property maturation from childhood to adulthood. *NeuroImage* 2022;**263**:119590.
- [20]. Ozkaya E, Fabris G, Macruz F et al. Viscoelasticity of children and adolescent brains through mr elastography. *J Mech Behav Biomed Mater* 2021;**115**:104229.
- [21]. Le Chen C, Hsu YC, Yang LY et al. Generalization of diffusion magnetic resonance imaging-based brain age prediction model through transfer learning. *NeuroImage* 2020;**217**:116831.
- [22]. Cole JH, Ritchie SJ, Bastin ME et al. Brain age predicts mortality. *Mol Psychiatry* 2018;**23**:1385–92.
- [23]. Jiang H, Lu N, Chen K et al. Predicting brain age of healthy adults based on structural MRI parcellation using convolutional neural networks. *Front Neurol* 2019;**10**:1346.
- [24]. Lund MJ, Alnæs D, de Lange AMG et al. Brain age prediction using FMRI network coupling in youths and associations with psychiatric symptoms. *Neuroimage Clin* 2022;**33**:102921.
- [25]. Mishra S, Beheshti I, Khanna P. A review of neuroimaging-driven brain age estimation for identification of brain disorders and health conditions. *IEEE Rev Biomed Eng* 2023;**16**:371–85.
- [26]. Baecker L, Garcia-Dias R, Vieira S et al. Machine learning for brain age prediction: introduction to methods and clinical applications. *EBioMedicine* 2021;**72**:103600.
- [27]. Lam PK, Santhalingam V, Suresh P et al. Accurate brain age prediction using recurrent slice-based networks. In: *16th International Symposium on Medical Information Processing and Analysis*, Vol. 11583, pp. 11–20. SPIE, 2020.
- [28]. Bellantuono L, Marzano L, La Rocca M et al. Predicting brain age with complex networks: from adolescence to adulthood. *NeuroImage* 2021;**225**:117458.
- [29]. Huang TW, Chen HT, Fujimoto R et al. Age estimation from brain MRI images using deep learning. In: *2017 IEEE 14th International Symposium on Biomedical Imaging*, pp. 849–52. Melbourne, VIC, Australia, 2017.
- [30]. Feng X, Lipton ZC, Yang J, Alzheimer's Disease Neuroimaging Initiative, Frontotemporal Lobar Degeneration Neuroimaging Initiative et al. Estimating brain age based on a uniform healthy population with deep learning and structural magnetic resonance imaging. *Neurobiol Aging* 2020;**91**:15–25.
- [31]. Shi W, Yan G, Li Y et al. Fetal brain age estimation and anomaly detection using attention-based deep ensembles with uncertainty. *NeuroImage* 2020;**223**:117316.
- [32]. Jónsson BA, Bjornsdottir G, Thorgeirsson TE et al. Brain age prediction using deep learning uncovers associated sequence variants. *Nat Commun* 2019;**10**:5409.
- [33]. Soumya Kumari LK, Sundarajan R. A review on brain age prediction models. *Brain Res* 2024;**1823**:148668.
- [34]. Tanveer M, Ganaie MA, Beheshti I et al. Deep learning for brain age estimation: a systematic review. *Information Fusion* 2023;**96**:130–43.
- [35]. El-Sappagh S, Abuhmed T, Kwak KS. Alzheimer disease prediction model based on decision fusion of cnn-bilstm deep neural networks. In: *Advances in Intelligent Systems and Computing*, Vol. 1252, pp. 482–92. AISC, 2020.
- [36]. Gupta H, Jin KH, Nguyen HQ et al. CNN-based projected gradient descent for consistent CT image reconstruction. *IEEE Trans Med Imaging* 2018;**37**:1440–53.
- [37]. Moeskops P, Viergever MA, Mendrik AM et al. Automatic segmentation of MR brain images with a convolutional neural network. *IEEE Trans Med Imaging* 2016;**35**:1252–61.
- [38]. Rehman A, Khan MA, Saba T et al. Microscopic brain tumor detection and classification using 3D CNN and feature selection architecture. *Microsc Res Tech* 2021;**84**:133–49.
- [39]. He K, Zhang X, Ren S, Sun J. Deep residual learning for image recognition. In: *2016 IEEE Conference on Computer Vision and Pattern Recognition (CVPR)*, Las Vegas, NV, USA, pp. 770–8, 2016.
- [40]. Peng H, Gong W, Beckmann CF et al. Accurate brain age prediction with lightweight deep neural networks. *Med Image Anal* 2021;**68**:101871.
- [41]. Wang Z, Yang J. Diabetic retinopathy detection via deep convolutional networks for discriminative localization and visual explanation. In: *Workshops at the Thirty-second AAAI Conference on Artificial Intelligence*, New Orleans, LA, USA, 2018.
- [42]. Hiscox LV, McGarry MDJ, Schwarb H et al. Standard-space atlas of the viscoelastic properties of the human brain. *Hum Brain Mapp* 2020;**41**:5282–300.
- [43]. Delgorio PL, Hiscox LV, Daugherty AM et al. Structure-function dissociations of human hippocampal subfield stiffness and memory performance. *J Neurosci* 2022;**42**:7957–68.
- [44]. Sanjana F, Delgorio PL, Hiscox LV et al. Blood lipid markers are associated with hippocampal viscoelastic properties and memory in humans. *J Cereb Blood Flow Metab* 2021;**41**:1417–27.
- [45]. Schneider JM, McIlvain G, Johnson CL. Mechanical properties of the developing brain are associated with language input and vocabulary outcome. *Dev Neuropsychol* 2022;**47**:258–72.
- [46]. Bayly PV, Alshareef A, Knutsen AK et al. Mr imaging of human brain mechanics in vivo: new measurements to facilitate the development of computational models of brain injury. *Ann Biomed Eng* 2021;**49**:2677–92.

- [47]. Johnson CL, Holtrop JL, McGarry MDJ et al. 3d multislabs, multishot acquisition for fast, whole-brain mr elastography with high signal-to-noise efficiency. *Magn Reson Med* 2014; **71**:477–85.
- [48]. Johnson CL, Holtrop JL, Anderson AT, Sutton BP. Brain MR elastography with multiband excitation and nonlinear motion-induced phase error correction. In: *Annual Meeting of the International Society for Magnetic Resonance in Medicine*, Singapore, 2016.
- [49]. McIlvain G, Cerjanic AM, Christodoulou AG et al. Oscillate: a low-rank approach for accelerated magnetic resonance elastography. *Magn Reson Med* 2022; **88**:1659–72.
- [50]. McIlvain, Matthew G, McGarry DJ, Johnson C,L, Johnson CL. Quantitative effects of off-resonance related distortion on brain mechanical property estimation with magnetic resonance elastography. *NMR Biomed* 2022; **35**:e4616.
- [51]. McGarry MDJ, van Houten EEW, Johnson CL et al. Multiresolution MR elastography using nonlinear inversion. *Med Phys* 2012; **39**:6388–96.
- [52]. Manduca A, Oliphant TE, Dresner MA et al. Magnetic resonance elastography: non-invasive mapping of tissue elasticity. *Med Image Anal* 2001; **5**:237–54.
- [53]. McGarry MDJ, van Houten EEW. Use of a rayleigh damping model in elastography. *Med Biol Eng Comput* 2008; **46**:759–66.
- [54]. Jenkinson M, Beckmann CF, Behrens TEJ et al. Fsl. *NeuroImage* 2012; **62**:782–90.
- [55]. Jenkinson M, Bannister P, Brady M, Smith S. Improved optimization for the robust and accurate linear registration and motion correction of brain images. *NeuroImage* 2002; **17**:825–41.
- [56]. Andersson JLR, Jenkinson M, Smith S. Non-linear registration aka spatial normalisation FMRIB technical report tr07ja2. Technical Report 1, FMRIB Analysis Group of the University of Oxford, 2007.
- [57]. Ashburner J, Friston KJ. Voxel-based morphometry—the methods. *NeuroImage* 2000; **11**:805–21.
- [58]. Smith SM, Jenkinson M, Woolrich MW et al. Advances in functional and structural MR image analysis and implementation as fsl. *NeuroImage* 2004; **23 Suppl 1**:S208–S219.
- [59]. Smith CD, Chebrolu H, Wekstein DR et al. Age and gender effects on human brain anatomy: a voxel-based morphometric study in healthy elderly. *Neurobiol Aging* 2007; **28**:1075–87.
- [60]. Taki Y, Goto R, Evans A et al. Voxel-based morphometry of human brain with age and cerebrovascular risk factors. *Neurobiol Aging* 2004; **25**:455–63.
- [61]. Tisserand DJ, van Boxtel MPJ, Pruessner JC et al. A voxel-based morphometric study to determine individual differences in gray matter density associated with age and cognitive change over time. *Cerebral Cortex* 2004; **14**:966–73.
- [62]. Zhang Y, Brady M, Smith S. Segmentation of brain MR images through a hidden Markov random field model and the expectation-maximization algorithm. *IEEE Trans Med Imaging* 2001; **20**:45–57.
- [63]. He K, Zhang X, Ren S, Sun J. Identity mappings in deep residual networks. In: *Computer Vision—ECCV 2016: 14th European Conference, Amsterdam, The Netherlands, October 11–14, 2016, Proceedings, Part IV 14*, pp. 630–45. Springer, 2016.
- [64]. Watanabe S. Tree-structured Parzen estimator: understanding its algorithm components and their roles for better empirical performance. *arXiv, preprint, arXiv:2304.11127*, 2023.
- [65]. Zou H, Hastie T. Regularization and variable selection via the elastic net. *J Roy Stat Soc Ser B Stat Methodol* 2005; **67**:301–20.
- [66]. Breiman L. *Random Forests*. *Machine Learning* 2001; **45**:5–32.
- [67]. Meng X, Jiang R, Lin D et al. Predicting individualized clinical measures by a generalized prediction framework and multi-modal fusion of MRI data. *NeuroImage* 2017; **145**:218–29.
- [68]. Asim Y, Raza B, Malik AK et al. A multi-modal, multi-atlas-based approach for Alzheimer detection via machine learning. *Int J Imaging Syst Tech* 2018; **28**:113–23.
- [69]. Yaakub SN, Heckemann RA, Keller SS et al. On brain atlas choice and automatic segmentation methods: a comparison of maper & freesurfer using three atlas databases. *Sci Rep* 2020; **10**:2837.
- [70]. Litwińczuk MC, Muhlert N, Trujillo-Barreto N, Woollams A. Impact of brain parcellation on prediction performance in models of cognition and demographics. *Hum Brain Mapp* 2024; **45**:e26592.
- [71]. Varikuti DP, Genon S, Sotiras A et al. Evaluation of non-negative matrix factorization of grey matter in age prediction. *NeuroImage* 2018; **173**:394–410.
- [72]. Eickhoff CR, Hoffstaedter F, Caspers J et al. Advanced brain ageing in Parkinson’s disease is related to disease duration and individual impairment. *Brain Commun* 2021; **3**:fcab191.
- [73]. More S, Antonopoulos G, Hoffstaedter F, Alzheimer’s Disease Neuroimaging Initiative et al. Brain-age prediction: a systematic comparison of machine learning workflows. *NeuroImage* 2023; **270**:119947.
- [74]. Lawrence RM, Bridgeford EW, Myers PE et al. Standardizing human brain parcellations. *Sci Data* 2021; **8**:78.
- [75]. Gorgolewski KJ, Varoquaux G, Rivera G et al. Neurovault.org: a web-based repository for collecting and sharing unthresholded statistical maps of the human brain. *Front Neuroinform* 2015; **9**:8.
- [76]. Jolliffe IT. *Principal Component Analysis for Special Types of Data*. Springer, 2002.
- [77]. Lee DD, Seung HS. Learning the parts of objects by non-negative matrix factorization. *Nature* 1999; **401**:788–91.
- [78]. Yang Z, Yuan Z, Laaksonen J. Projective non-negative matrix factorization with applications to facial image processing. *Int J Patt Recogn Artif Intell* 2007; **21**:1353–62.
- [79]. Yang Z, Oja E. Linear and nonlinear projective nonnegative matrix factorization. *IEEE Trans Neural Netw* 2010; **21**:734–49.
- [80]. Sotiras A, Resnick SM, Davatzikos C. Finding imaging patterns of structural covariance via non-negative matrix factorization. *NeuroImage* 2015; **108**:1–16.
- [81]. Sotiras A, Toledo JB, Gur RE et al. Patterns of coordinated cortical remodeling during adolescence and their associations with functional specialization and evolutionary expansion. *Proc Natl Acad Sci USA* 2017; **114**:3527–32.
- [82]. Ha SM, Bani A, Sotiras A. Scalable NMF via linearly optimized data compression. In: *Proceedings of SPIE—the International Society for Optical Engineering*, San Diego, CA, USA, 12464:124640V, 2023.
- [83]. Franke K, Ziegler G, Klöppel S, Gaser C, Alzheimer’s Disease Neuroimaging Initiative. Estimating the age of healthy subjects from t1-weighted MRI scans using kernel methods: exploring the influence of various parameters. *NeuroImage* 2010; **50**:883–92.
- [84]. Franke K, Luders E, May A et al. Brain maturation: predicting individual brainage in children and adolescents using structural mri. *NeuroImage* 2012; **63**:1305–12.
- [85]. Xifra-Porxas A, Ghosh A, Mitsis GD, Boudrias M-H. Estimating brain age from structural MRI and MEG data: insights from dimensionality reduction techniques. *NeuroImage* 2021; **231**:117822.
- [86]. Breiman L. Bagging predictors. *Mach Learn* 1996; **24**:123–40.



- [87]. Dietterich TG. Ensemble methods in machine learning. In *International Workshop on Multiple Classifier Systems*, pp. 1–15. Springer, 2000.
- [88]. Selvaraju RR, Cogswell M, Das A et al. Grad-cam: visual explanations from deep networks via gradient-based localization. In: *2017 IEEE International Conference on Computer Vision (ICCV)*, Venice, Italy, pp. 618–26, 2017.
- [89]. Chattopadhyay A, Sarkar A, Howlader P, Balasubramanian VN. Grad-cam++: generalized gradient-based visual explanations for deep convolutional networks. In: *2018 IEEE Winter Conference on Applications of Computer Vision (WACV)*, pp. 839–47. IEEE, 2018.
- [90]. Lea Draelos R, Carin L. Use hirescam instead of grad-cam for faithful explanations of convolutional neural networks. *arXiv preprint arXiv:2011.08891*, 2020.
- [91]. Makris N, Goldstein JM, Kennedy D et al. Decreased volume of left and total anterior insular lobule in schizophrenia. *Schizophr Res* 2006;**83**:155–71.
- [92]. Frazier JA, Chiu S, Breeze JL et al. Structural brain magnetic resonance imaging of limbic and thalamic volumes in pediatric bipolar disorder. *Am J Psychiatry* 2005;**162**:1256–65.
- [93]. Desikan RS, Ségonne F, Fischl B et al. An automated labeling system for subdividing the human cerebral cortex on MRI scans into gyral based regions of interest. *Neuroimage* 2006;**31**:968–80.
- [94]. Goldstein JM, Seidman LJ, Makris N et al. Hypothalamic abnormalities in schizophrenia: sex effects and genetic vulnerability. *Biol Psychiatry* 2007;**61**:935–45.
- [95]. Sack I, Jöhrens K, Würfel J, Braun J. Structure-sensitive elastography: on the viscoelastic powerlaw behavior of in vivo human tissue in health and disease. *Soft Matter* 2013;**9**:5672–80.
- [96]. Johnson CL, Schwarb H, Horecka KM et al. Double dissociation of structure-function relationships in memory and fluid intelligence observed with magnetic resonance elastography. *Neuroimage* 2018;**171**:99–106.
- [97]. Schwarb H, Johnson CL, McGarry MDJ, Cohen NJ. Medial temporal lobe viscoelasticity and relational memory performance. *NeuroImage* 2016;**132**:534–41.
- [98]. Schaffer C. A conservation law for generalization performance. In: *Machine Learning Proceedings 1994*, pp. 259–65. Elsevier, 1994.
- [99]. Wolpert DH. The lack of a priori distinctions between learning algorithms. *Neural Comput* 1996;**8**:1341–90.
- [100]. Shalev-Shwartz, S Ben-David S. *Understanding Machine Learning: From Theory to Algorithms*. Cambridge University Press, 2014.
- [101]. Shen D, Wu G, Suk H-I. Deep learning in medical image analysis. *Annu Rev Biomed Eng* 2017;**19**:221–48.
- [102]. Litjens G, Kooi T, Bejnordi BE et al. A survey on deep learning in medical image analysis. *Med Image Anal* 2017;**42**:60–88.
- [103]. Hinton G. Deep learning—a technology with the potential to transform health care. *JAMA* 2018;**320**:1101–2.
- [104]. Greenspan H, Van Ginneken B, Summers RM. Guest editorial deep learning in medical imaging: overview and future promise of an exciting new technique. *IEEE Trans Med Imaging* 2016;**35**:1153–9.
- [105]. Yan W, Qu G, Hu W et al. Deep learning in neuroimaging: promises and challenges. *IEEE Signal Process Mag* 2022;**39**:87–98.
- [106]. Vieira S, Pinaya WH, Mechelli A. Using deep learning to investigate the neuroimaging correlates of psychiatric and neurological disorders: methods and applications. *Neurosci Biobehav Rev* 2017;**74**:58–75.
- [107]. Plis SM, Hjelm DR, Salakhutdinov R et al. Deep learning for neuroimaging: a validation study. *Front Neurosci* 2014;**8**:229.
- [108]. Abrol A, Bhattarai M, Fedorov A, Alzheimer’s Disease Neuroimaging Initiative et al. Deep residual learning for neuroimaging: an application to predict progression to Alzheimer’s disease. *J Neurosci Methods* 2020;**339**:108701.
- [109]. Oh K, Chung Y-C, Kim KW et al. Classification and visualization of Alzheimer’s disease using volumetric convolutional neural network and transfer learning. *Sci Rep* 2019;**9**:18150.
- [110]. Cole JH, Poudel RP, Tsagkrasoulis D et al. Predicting brain age with deep learning from raw imaging data results in a reliable and heritable biomarker. *NeuroImage* 2017;**163**:115–24.
- [111]. Fedorov A, Hjelm RD, Abrol A et al. Prediction of progression to Alzheimer’s disease with deep infomax. In: *2019 IEEE EMBS International Conference on Biomedical & Health Informatics (BHI)*, pp. 1–5. IEEE, 2019.
- [112]. Abrol A, Fu Z, Du Y, Calhoun VD. Multimodal data fusion of deep learning and dynamic functional connectivity features to predict Alzheimer’s disease progression. In: *2019 41st Annual International Conference of the IEEE Engineering in Medicine and Biology Society (EMBC)*, pp. 4409–13. IEEE, 2019.
- [113]. Abrol A, Rokham H, Calhoun VD. Diagnostic and prognostic classification of brain disorders using residual learning on structural mri data. In: *2019 41st Annual International Conference of the IEEE Engineering in Medicine and Biology Society (EMBC)*, pp. 4084–8. IEEE, 2019.
- [114]. Leonardsen EH, Peng H, Kaufmann T et al. Deep neural networks learn general and clinically relevant representations of the ageing brain. *NeuroImage* 2022;**256**:119210.
- [115]. Cherubini A, Caligiuri ME, Péran P et al. Importance of multimodal MRI in characterizing brain tissue and its potential application for individual age prediction. *IEEE J Biomed Health Inform* 2016;**20**:1232–9.
- [116]. Hugenschmidt CE, Peiffer AM, Kraft RA et al. Relating imaging indices of white matter integrity and volume in healthy older adults. *Cerebral Cortex* 2008;**18**:433–42.
- [117]. Raz N, Ghisletta P, Rodrigue KM et al. Trajectories of brain aging in middle-aged and older adults: regional and individual differences. *Neuroimage* 2010;**51**:501–11.
- [118]. Scahill RI, Frost C, Jenkins R et al. A longitudinal study of brain volume changes in normal aging using serial registered magnetic resonance imaging. *Arch Neurol* 2003;**60**:989–94.
- [119]. Schmidt R, Schmidt H, Haybaeck J et al. Heterogeneity in age-related white matter changes. *Acta Neuropathol* 2011;**122**:171–85.
- [120]. Mhaskar H, Liao Q, Poggio T. When and why are deep networks better than shallow ones? In: *Proceedings of the AAAI Conference on Artificial Intelligence*, Vol. 31, San Francisco, CA, USA, 2017.
- [121]. Wang Z, Wu L. Theoretical analysis of the inductive biases in deep convolutional networks. *Adv Neural Infor Process Syst* 2024;**36**:74289–338.
- [122]. He F, Liu T, Tao D. Why resnet works? Residuals generalize. *IEEE Trans Neural Netw Learn Syst* 2020;**31**:5349–62.
- [123]. Simon IV J, Rudebeck PH, Rich EL. From affective to cognitive processing: functional organization of the medial frontal cortex. In: *International Review of Neurobiology*, Vol. 158, pp. 1–28. Elsevier, 2021.
- [124]. MacPherson SE, Phillips LH, Della Sala S. Age, executive function and social decision making: a dorsolateral prefrontal theory of cognitive aging. *Psychol Aging* 2002;**17**:598–609.

- [125]. Winecoff A, LaBar KS, Madden DJ et al. Cognitive and neural contributors to emotion regulation in aging. *Soc Cogn Affect Neurosci* 2011;**6**:165–76.
- [126]. Sowell ER, Delis D, Stiles J, Jernigan TL. Improved memory functioning and frontal lobe maturation between childhood and adolescence: a structural MRI study. *J Int Neuropsychol Soc* 2001;**7**:312–22.
- [127]. Butler PM, Chiong W. Neurodegenerative disorders of the human frontal lobes. *Handb Clin Neurol* 2019;**163**:391–410.
- [128]. Koziol LF, Budding DE. *Subcortical Structures and Cognition: Implications for Neuropsychological Assessment*. Springer, 2009.
- [129]. Groeschel S, Vollmer B, King MD, Connelly A. Developmental changes in cerebral grey and white matter volume from infancy to adulthood. *Int J Dev Neurosci* 2010;**28**:481–9.
- [130]. Fogassi L, Ferrari PF, Gesierich B et al. Parietal lobe: from action organization to intention understanding. *Science* 2005;**308**:662–7.
- [131]. Gennatas ED, Avants BB, Wolf DH et al. Age-related effects and sex differences in gray matter density, volume, mass, and cortical thickness from childhood to young adulthood. *J Neurosci* 2017;**37**:5065–73.
- [132]. Mabbott DJ, Noseworthy M, Bouffet E et al. White matter growth as a mechanism of cognitive development in children. *NeuroImage* 2006;**33**:936–46.
- [133]. Guttmann CRG, Jolesz FA, Kikinis R et al. White matter changes with normal aging. *Neurology* 1998;**50**:972–8.
- [134]. Terry RD, DeTeresa R, Hansen LA. Neocortical cell counts in normal human adult aging. *Ann Neurol* 1987;**21**:530–9.
- [135]. Vernooij MW, de Groot M, van der Lugt A et al. White matter atrophy and lesion formation explain the loss of structural integrity of white matter in aging. *NeuroImage* 2008;**43**:470–7.
- [136]. Freimann FB, Müller S, Streitberger KJ et al. MR elastography in a murine stroke model reveals correlation of macroscopic viscoelastic properties of the brain with neuronal density. *NMR Biomed* 2013;**26**:1534–9.
- [137]. Schregel K, Wuerfel E, Garteiser P et al. Demyelination reduces brain parenchymal stiffness quantified in vivo by magnetic resonance elastography. *Proc Natl Acad Sci U S A* 2012;**109**:6650–5.
- [138]. Weickenmeier J, de Rooij R, Budday S et al. Brain stiffness increases with myelin content. *Acta Biomater* 2016;**42**:265–72.
- [139]. Gerischer LM, Fehlner A, Köbe T et al. Combining viscoelasticity, diffusivity and volume of the hippocampus for the diagnosis of Alzheimer's disease based on magnetic resonance imaging. *Neuroimage Clin* 2018;**18**:485–93.
- [140]. Murphy MC, Jones DT, Jack CR et al. Regional brain stiffness changes across the alzheimer's disease spectrum. *Neuroimage Clin* 2016;**10**:283–90.
- [141]. ElSheikh M, Arani A, Perry A et al. MR elastography demonstrates unique regional brain stiffness patterns in dementias. *Ajr Am J Roentgenol* 2017;**209**:403–8.
- [142]. Pavuluri KD, Scott JM, Huston J et al. Differential effect of dementia etiology on cortical stiffness as assessed by mr elastography. *Neuroimage Clin* 2023;**37**:103328.
- [143]. Guo J, Hirsch S, Fehlner A et al. Towards an elastographic atlas of brain anatomy. *Plos ONE* 2013;**8**:e71807.